



**HAL**  
open science

# Computational Design of Pd Nanocluster and Pd Single-Atom Catalysts Supported on O-Functionalized Graphene

Javier Navarro-Ruiz, Camila Rivera-Cárcamo, Bruno Machado, Philippe Serp, Iker Del rosál, I.C. Gerber

► **To cite this version:**

Javier Navarro-Ruiz, Camila Rivera-Cárcamo, Bruno Machado, Philippe Serp, Iker Del rosál, et al.. Computational Design of Pd Nanocluster and Pd Single-Atom Catalysts Supported on O-Functionalized Graphene. ACS Applied Nano Materials, 2021, 4 (11), pp.12235-12249. 10.1021/ac-sanm.1c02743 . hal-03627539

**HAL Id: hal-03627539**

<https://insa-toulouse.hal.science/hal-03627539v1>

Submitted on 1 Apr 2022

**HAL** is a multi-disciplinary open access archive for the deposit and dissemination of scientific research documents, whether they are published or not. The documents may come from teaching and research institutions in France or abroad, or from public or private research centers.

L'archive ouverte pluridisciplinaire **HAL**, est destinée au dépôt et à la diffusion de documents scientifiques de niveau recherche, publiés ou non, émanant des établissements d'enseignement et de recherche français ou étrangers, des laboratoires publics ou privés.

# Computational Design of Pd Nanocluster and Pd Single-Atom Catalysts Supported on O- Functionalized Graphene

*Javier Navarro-Ruiz,<sup>†</sup> Camila Rivera-Cárcamo,<sup>‡</sup> Bruno Machado,<sup>□</sup> Philippe Serp,<sup>‡</sup> Iker del  
Rosal,<sup>†</sup> and Iann C. Gerber<sup>\*,†</sup>*

<sup>†</sup> LPCNO, Université de Toulouse, INSA–CNRS–UPS, 135 Avenue de Rangueil, F-31077  
Toulouse, Cedex 4, France

<sup>‡</sup> LCC–CNRS, Université de Toulouse, INPT, 205 Route de Narbonne, F-31077 Toulouse,  
Cedex 4, France

<sup>□</sup> LSRE–LCM, Chemical Engineering Department, Faculty of Engineering, University of Porto,  
Rua Dr. Roberto Frias s/n, 4200-465 Porto, Portugal

**ABSTRACT:** A crucial step in the preparation of supported metal catalysts is related to the choice of support, since it regulates the anchoring of the metal species in an environment of strong interaction. In this sense, the binding on the support, which may present defects, as well as induced modifications of the electronic structure, help to determine efficient metal/support combinations for catalysis applications. In this work, first-principles studies have been carried out to model and describe the geometric and electronic properties of an O-functionalized graphene as a model carbon support, in addition to single Pd atom and Pd<sub>13</sub> nanocluster (experimentally observed on various carbon supports) as supported metal catalysts. The carbon-based nanomaterial includes experimentally probed abundant oxygen functional groups and point defects, demonstrating high thermal stability at room temperature. The characterization confirms the structural motifs presented in the model, distinguishing the organic functionalities and various defects by spectroscopy techniques. Interestingly, the oxygenated carbon-based support presents a metallic character when the formal charges of the embedded Pd atom and nanocluster have been determined to be [Pd]<sup>+</sup> and [Pd<sub>13</sub>]<sup>3+</sup>. The hydrogenation process of the adsorbed cluster is also presented, with the determination of a ratio between the adsorbed hydrides and the surface metal atoms close to unity at room temperature, thanks to *ab initio* molecular dynamics.

**KEYWORDS:** Palladium, nanocluster, single atom, supported catalyst, oxygen functional group, graphene, hydrogenation

## 1. INTRODUCTION

Supported-metal catalysts are among the most important materials in heterogeneous catalysis.<sup>1</sup> Consisting of single atoms (SA), clusters, and/or nanoparticles (NP) anchored onto solid supports, these materials can maintain the advantages of molecular catalysts (often highly active/selective) and minimize their disadvantages (expensive catalyst separation from products and corrosion-related damage), thus allowing their use in industrial processes.<sup>2</sup> To do this, the system under consideration (usually metal NP) must be in a sufficiently high dispersed form.<sup>3</sup>

The active metal component is usually deposited on the surface of a porous solid support, a thermally/mechanically stable material, which is able to maintain the catalyst life, but also to disperse the metal and prevent its agglomeration.<sup>3</sup> The catalyst supports can be inert or active in the catalytic reactions and can cooperate with the metal, for example via spillover.<sup>4</sup> Importantly, electronic and geometric effects induced by the support contribute to control catalyst performances (activity, selectivity, and stability), especially in highly dispersed catalysts, for which the metal-support interaction is decisive.<sup>5,6</sup> Typical support materials include metal oxides, zeolites, and various carbon nanomaterials.<sup>7</sup> Carbon-supported metal catalysts are employed in a large number of industrial reactions including oil refining, hydrogenation, and oxidation, as well as for electrocatalysis.<sup>8</sup>

Several carbon-based (nano)materials can be used as catalyst support: (i) 0D (NP); (ii) 1D (carbon nanotubes, CNTs); (iii) 2D (graphene sheets); and (iv) 3D (mesoporous carbons, MC).<sup>9</sup> Due to the unique lattice structure and physicochemical properties of (few-layer) graphene, this material has been particularly studied as catalyst support,<sup>10</sup> both for metal NP and metal SA.<sup>11</sup> Nevertheless, most of the produced graphene sheets are not perfect, presenting defects (intrinsic

or due to the presence of a foreign atom) that influence their physical, mechanical, and even electronic properties. Besides the intrinsic defects [Stone-Wales (SW) and vacancies],<sup>12</sup> chemical doping can modify graphene properties and induce specific sites, which contribute to different catalytic performance. Among the various potential dopants, oxygen is considered as an excellent element for chemical doping of carbon-based (nano)materials. These O-doped materials are usually produced with strong oxidizing agents in acidic media to introduce oxygenated functional groups (OFG) comprising carboxylic acids, esters, ketones, phenols, lactones, lactols, or quinones.<sup>13</sup> O-functionalized graphene can be represented with a simplified model consisting of individual graphene sheet ( $sp^2$  carbon atoms)<sup>14</sup> decorated with OFG on both the basal planes and edges,<sup>15</sup> resulting in a carbon network having both  $sp^2$ - and  $sp^3$ -hybridized carbons bearing OFG.<sup>16</sup> However, currently the precise atomic and electronic structure of O-functionalized graphene sheets remains largely unknown. This is mainly due to the uncertainty related to the amount and types of OFG,<sup>17</sup> and their nonstoichiometric atomic composition. Owing to these OFG, the materials exhibit an amphoteric (acid–base) character that improves metal adsorption and dispersion, resulting in mixtures of metal NP and SA, which have been observed on commercial catalysts.<sup>18</sup> When such catalysts are used for hydrogenation reactions, hydrogen spillover can also operate. It is also promoted by the presence of OFG on the carbon surface, and examples of cooperative catalysis between metal NP and metal SA thanks to H-spillover on the carbon support have been reported.<sup>19</sup> The understanding of the chemical reactivity of such complex systems definitively requires robust models.

Theoretical simulations can provide remarkable insight into the possible thermodynamic and kinetic mechanisms required for a greater understanding on the structure of OFG found on carbon nanomaterials and on their influence on the reactivity of metal species.<sup>20</sup> Nowadays,

endeavors are directed towards simple schemes that allow for basic structural motifs using common oxygen groups, specifically hydroxyl and 1,2-ethers (epoxide).<sup>21,22</sup> Thus, the aim of the present work is: i) to design, based on *ab initio* electronic structure methods, a more realistic O-functionalized support mainly based on experimental data; and ii) to provide a detailed description of different physicochemical features of the modified support and suggested supported palladium catalysts (Pd/C is a very common hydrogenation catalyst). In particular, analysis of the structural (average bond length, mean coordination number, and mean interatomic distances), electronic (density of states, crystal orbital Hamilton population, and Mulliken population analysis), and vibrational (infrared and Raman spectra) properties are presented. Special attention to the differences between single-atom and cluster-containing catalysts is also addressed.

## 2. COMPUTATIONAL DETAILS

Periodic density functional theory (DFT) calculations were performed using the *ab initio* plane-wave pseudopotential approach as implemented in the Vienna Ab initio Simulation Package (VASP; version 5.4).<sup>23,24</sup> The Perdew–Burke–Ernzerhof<sup>25</sup> exchange–correlation functional within the generalized gradient approximation was chosen, and van der Waals interactions were taken into account through the D3 correction method of Grimme *et al.*<sup>26</sup> The innermost electrons were replaced by a projector-augmented wave (PAW) approach,<sup>27,28</sup> while the valence monoelectronic states were expanded in a plane-wave basis set with a cut-off energy of 450 eV. Partial occupancies were estimated with a Gaussian smearing ( $\sigma$ ) of 0.05 eV during all relaxations and extrapolating the energies to  $\sigma = 0.00$  eV, except for the determination of the electronic density of states (DOS) for which the tetrahedron method with Blöchl corrections was used. The carbon support was modelled as a graphene slab, showing that a  $(7 \times 7)$  supercell was found to be large enough to include a broad representation of experimentally observed OFG. The  $(7 \times 7)$  unit cell contains 98

C atoms and a  $\Gamma$ -centered ( $3 \times 3 \times 1$ )  $k$ -point grid generated using the Monkhorst-Pack method<sup>29</sup> was employed as a good compromise between accuracy and computational cost. A higher density of  $k$ -points and energy cut-off were used in obtaining DOS calculations for all the structures considered for the present study. All of the systems considered are neutral. Spurious interactions between the modelled slab and its periodic images perpendicular to the slab were eliminated by introducing a vacuum region by at least 10 Å, and by applying a dipole correction to the total energy along the  $z$ -direction. Iterative relaxation of atomic positions proceeded until the change in total energy between successive steps was less than  $10^{-6}$  eV per cell and the residual forces on any direction acting on the atoms (evaluated using the conjugate-gradient algorithm) were less than  $0.015 \text{ eV \AA}^{-1}$ .

To probe the thermal stability of some of the systems, first-principle Born-Oppenheimer *ab initio* molecular dynamics simulations (AIMD) were performed within the canonical NVT ensemble (that is, constant number of particles, the system's volume, and the temperature). Starting from the optimized structure, each slab was propagated at 298 K for 20 picoseconds at time steps of 0.5 femtoseconds for integrating the atomic equations of motion. The level of theory was the same as described above and the  $k$ -mesh was reduced to a gamma point. In all cases, the electronic structures were well converged to  $10^{-6}$  eV. The temperature was regulated by the Nosé thermostat.<sup>30</sup>

To provide additional insight on the modelled support, as well as the interactions between the metal catalysts and the support itself, the Crystal Orbital Hamilton Population (COHP) analysis<sup>33</sup> is performed with the LOBSTER package.<sup>31,32</sup> Based on contributions from orbital pairs, COHP is an energy division of the band structure, so it acts on a local basis. In this regard, from a plane-wave DFT output, the LOBSTER package allows calculating the projected COHP in a local

atomic base set (pCOHP) as well as a consistent density of states projected by atoms (pDOS). The COHP analysis is performed for pairs of atoms at distances according to the nearest neighbor, and subsequently the COHP is plotted by accumulating all the pairs with the same elements. To demonstrate the contributions of different elements, the pDOS and pCOHP plots are shown together. The charge spilling (a measure that assesses the quality of the projection) for all the compounds of this work reaches a maximum value of 2%. Furthermore, for particular cases the integrated pCOHP (IpCOHP) was calculated, providing qualitative data on the average bond strength in covalent entities.

Vibrational frequencies of the ground-state geometries were determined from phonon calculations by diagonalizing the numerical Hessian matrix (VASP calculates phonons at the zone-center  $\Gamma$ -point within the supercell approach). The elements of the Hessian matrix (harmonic approximation) were calculated by finite differences of the analytical first derivatives of the energy with respect to atomic displacements using the central-difference formula, in which each atom is displaced using small steps of 0.015 Å in both positive and negative directions of each coordinate to estimate the harmonic potentials. The value of the infrared (IR) intensities for each normal mode was also computed by performing linear response calculations within density-functional perturbation theory (DFPT) formalism. From the Born effective charge (BEC) tensor, which refers to the change in polarizability of atoms with respect to an external electric field, the vibrational intensities of the modes were calculated using the formula by Giannozzi and Baroni.<sup>34</sup> Additionally, for both the pristine and O-modified supports, the off-resonance Raman activity is calculated for each of the normal modes obtained, taking advantage of the derivative of the polarizability (or macroscopic dielectric tensor) with respect to the coordinates of the normal

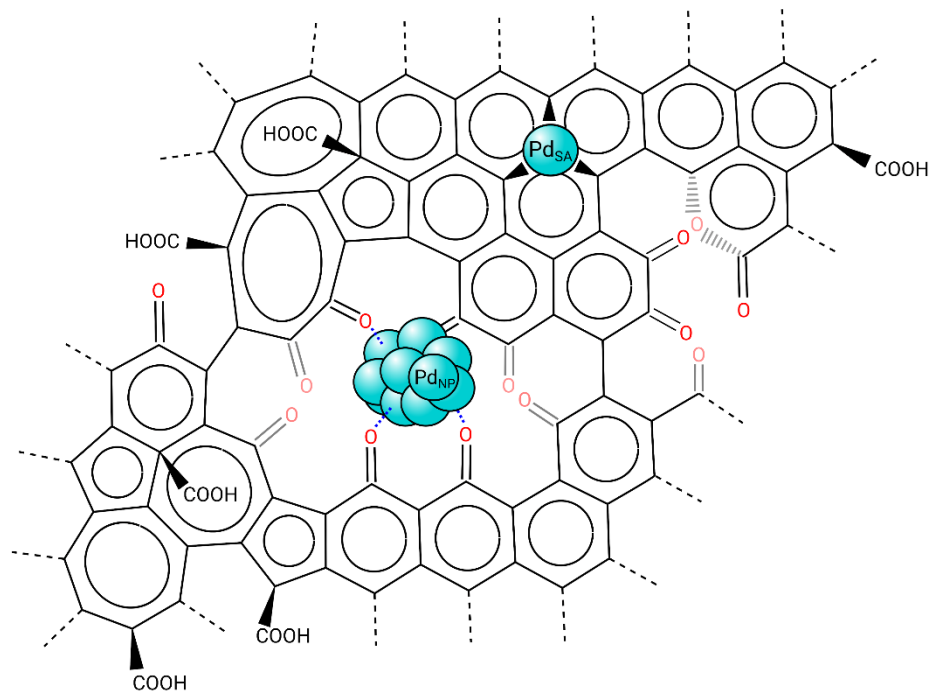
modes.<sup>35</sup> Therefore, from the phonon calculation at  $\Gamma$ -point and the macroscopic dielectric tensor of the previous DFPT, the non-resonant Raman scattering activities are computed.

### 3. RESULTS AND DISCUSSION

This section is organized as follows. First, results based on experimental data, related to the computational modelling of the oxygen-functionalized support from pristine graphene (G) are shown. Then, analyses on the structure-property, electronic structure, and vibrational of the support are provided from the density of states, partial atomic charges, and the IR and Raman spectra. Afterward, the anchoring of both a palladium single atom ( $\text{Pd}_{\text{SA}}$ ) and a Pd cluster ( $\text{Pd}_{\text{NP}}$ ) is discussed, paying special attention to the structural and electronic changes that occur both in the carbon support and in the metallic systems before and after metal deposition. Finally, the hydrogenation of the ultra-small  $\text{Pd}_{\text{NP}}$  is considered, discussing how this process affects the nature of the catalyst (the overall structure and chemical composition is provided in Scheme 1).

**Design of the support.** The first step in the development of supported metal catalysts is the design of the support. To this end, graphene was used as model carbon support (Figure 1a), given its excellent properties shown in supported catalysis.<sup>6</sup>

*Formation and reconstruction of vacancy defects.* Lattice imperfections are unavoidably introduced into graphene during its growth or processing. SW defect,<sup>36</sup> single and multiple vacancies (MV),<sup>37</sup> carbon, foreign adatoms,<sup>38</sup> and substitutional impurities<sup>39</sup> are typical stable graphene point defects that have been predicted. As a result, carbon atoms with a  $sp^2$  hybridization could undergo patterns other than hexagonal, leading to different systems. From a thermodynamic point of view, double vacancies (DV) appear as the most favored vacancy defects in graphene over single vacancies (SV).<sup>37</sup> The reconstruction in the former's atomic network allow a coherent



**Scheme 1.** Structure and chemical composition of the nanomaterials system.

defective lattice without under-coordinated atoms, and therefore with no dangling bonds. Furthermore, the removal of more than two atoms may lead to larger and more complex defect configurations.

As a consequence of the combination of two SV or elimination of two contiguous atoms, a DV can be formed, in which completely reconstructed DV with a pair of pentagonal and a single octagonal cells of carbon atoms [ $V_2(5-8-5)$  defect] appears. However, it is further reconstructed and transformed into a new defect structure by a SW type transformation [ $V_2(555-777)$  defect], consisting of three pentagonal and three heptagonal cells of carbon atoms in the graphene lattice.<sup>40</sup> From an energy point of view, the  $V_2(555-777)$  defect is much more stable than two isolated SV, its formation energy being lower than in the case of  $V_2(5-8-5)$ , of the order of 1 eV. This type of defect is also commonly noted in electron microscopy analyses.<sup>41</sup> For all these reasons, the introduction of two  $V_2(555-777)$  defects were firstly considered on pristine G, as revealed in Figure 1b. These defects did not cause any deformation in the surface plane.

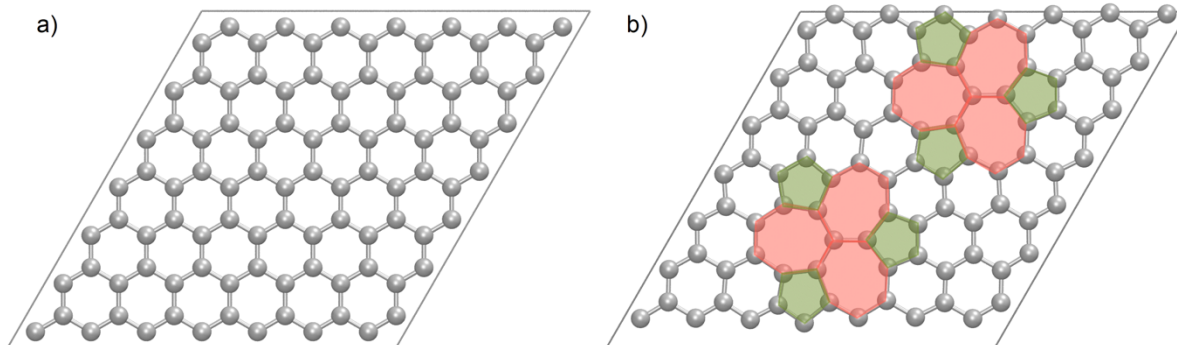


**Figure 1.** Pristine graphene (a) and doubly V<sub>2</sub>(555-777) defect (b) created in graphene.

*Addition of oxygen functional groups (OFG).* The reactivity of the carbon support is increased locally due to the presence of these point defects and allow surface functionalization. Therefore, the next step was to include OFG that can be experimentally detected and quantified.<sup>42</sup> For this purpose, Temperature Programmed Desorption (TPD) experiments in conjunction with Mass Spectroscopy (MS) measurements can be applied.<sup>43</sup> TPD-MS study is certainly a frequent technique for the description of the OFG on carbon materials, decomposing into CO/CO<sub>2</sub> and, on certain occasions, H<sub>2</sub>O at different temperatures. In our case, multi-walled carbon nanotubes (MWCNT) or few-layer graphene (FLG), which have been oxidized with nitric acid, were used as support. This procedure is commonly used on carbon supports prior to metal deposition to provide anchoring sites (OFG) for the metallic phase.<sup>44</sup> Full experimental details are described in the ESI and the progress of CO<sub>2</sub> and CO throughout TPD-MS studies under helium for the oxidized MWCNT (CNT<sub>ox</sub>) are shown on Figure S1. Taking into account the spectra of CO<sub>2</sub> and CO, it can be seen that the CNT<sub>ox</sub> support comprises carboxylic (CO<sub>2</sub> at 217/291 °C, peaks #1 and #2), carboxylic anhydride (CO<sub>2</sub> at 437 °C, peak #3 and CO at 491 °C, peak #1'), lactone (CO<sub>2</sub> at 576 °C, peak #4), phenol (CO at 717 °C, peak #2'), and carbonyl/quinone (CO at 882 °C, peak #3') surface groups (the deconvolution of CO<sub>2</sub> and CO profiles of CNT<sub>ox</sub> using a multiple Gaussian

function are shown in Figure S1 and the quantification in Table S1). Considering the specific surface area of CNT<sub>ox</sub> ( $S_{\text{BET}} = 220 \text{ m}^2 \text{ g}^{-1}$ ) and the fact that the hexagonal unit cell of graphene contains two carbon atoms having an area of  $0.052 \text{ nm}^2$ , so  $38.5 \text{ C nm}^{-2}$ , it was possible to calculate the density of OFG, as illustrated in Figure 2. For comparative purpose, the same procedure was followed for an oxidized FLG support. The comparison of the density of OFG obtained on CNT<sub>ox</sub> and FLG<sub>ox</sub> supports is shown on Figure S2, observing the same trends for both supports. It is logic to find few differences since the two supports do not present the same structure and should not have exactly the same reactivity towards the oxidant ( $\text{HNO}_3$ ).

In order to take into account each of the OFG, the modelling of the different groups was carried out by means of a sequence of serial optimizations on the defective graphene. The addition is made by functional groups, so that the support gradually adapts against oxidation. Firstly, the carboxylic acid groups are introduced. Since a carbon edge model was never considered, the acid function is irremediably located on top of the surface. Thus, different positions were tested (that is, on pentagonal, hexagonal and heptagonal cell carbons), the most stable being the one in which the  $-\text{COOH}$  motif is adsorbed on a carbon belonging to a five-membered ring. Due to the large number of motifs to take into account according to the high density, they were distributed in several successive sets (relaxing all from one to another). Secondly, the carbonyl groups were added in an analogous way (distribution in successive relaxations). Contrary to the acidic functional group, the carbonyl groups must be located at the edges. As mentioned, the support model does not explicitly consider carbon atoms at the edge of graphene, such as zigzag or armchair edges, which necessarily causes an increase in the size of the  $V_2(555-777)$  defects, going from two DV to two larger vacancies commonly known as MV.

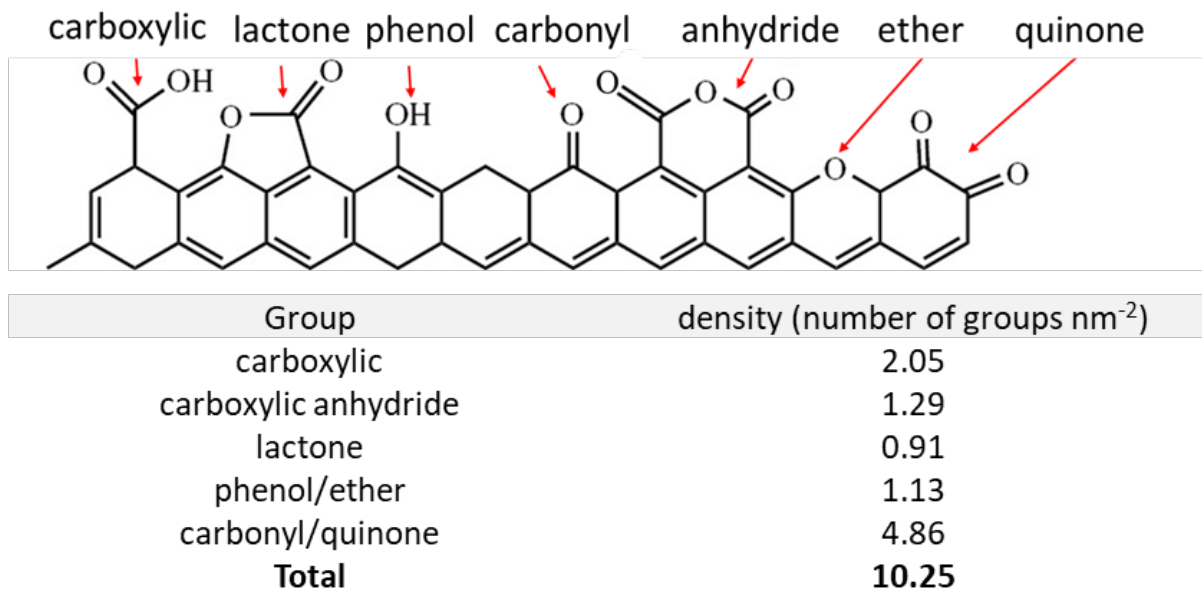


**Figure 2.** Schematic representation of the different oxygen functional groups (OFG) experimentally observed and their corresponding surface density.

Third and last, the rest of the functional groups of lower density were included at the same time, that is, phenol/ether, and lactone. For reasons of steric hindrance, the anhydride functional group was not taken into account during the design of the functionalized support. These last three functional groups must also be located on the edges of the graphene support. The final result of which can be seen in the left inset of Figure 3 (top and side views, a). Unsurprisingly, the largest MV (center of the unit cell) predominates in the support, although completely saturated by carbonyl and quinone groups. This high concentration of oxygenated groups in the MV induces the loss of the graphene planarity due to the electronic repulsion between the lone pairs of oxygen atoms, leading to the formation of surface corrugations. Finally, many experimental carbon-based catalysts use FLG and/or CNT as support. Thus, in order to validate the simplified support modelled by a single layer, a rhombohedral (ABC stacking order) trilayer graphene was carried out as a more realistic system (the atomistic structure is depicted in Figure S3). No significant structural or electronic changes were appreciated, apart from the new existing  $\pi$ - $\pi$  stacking

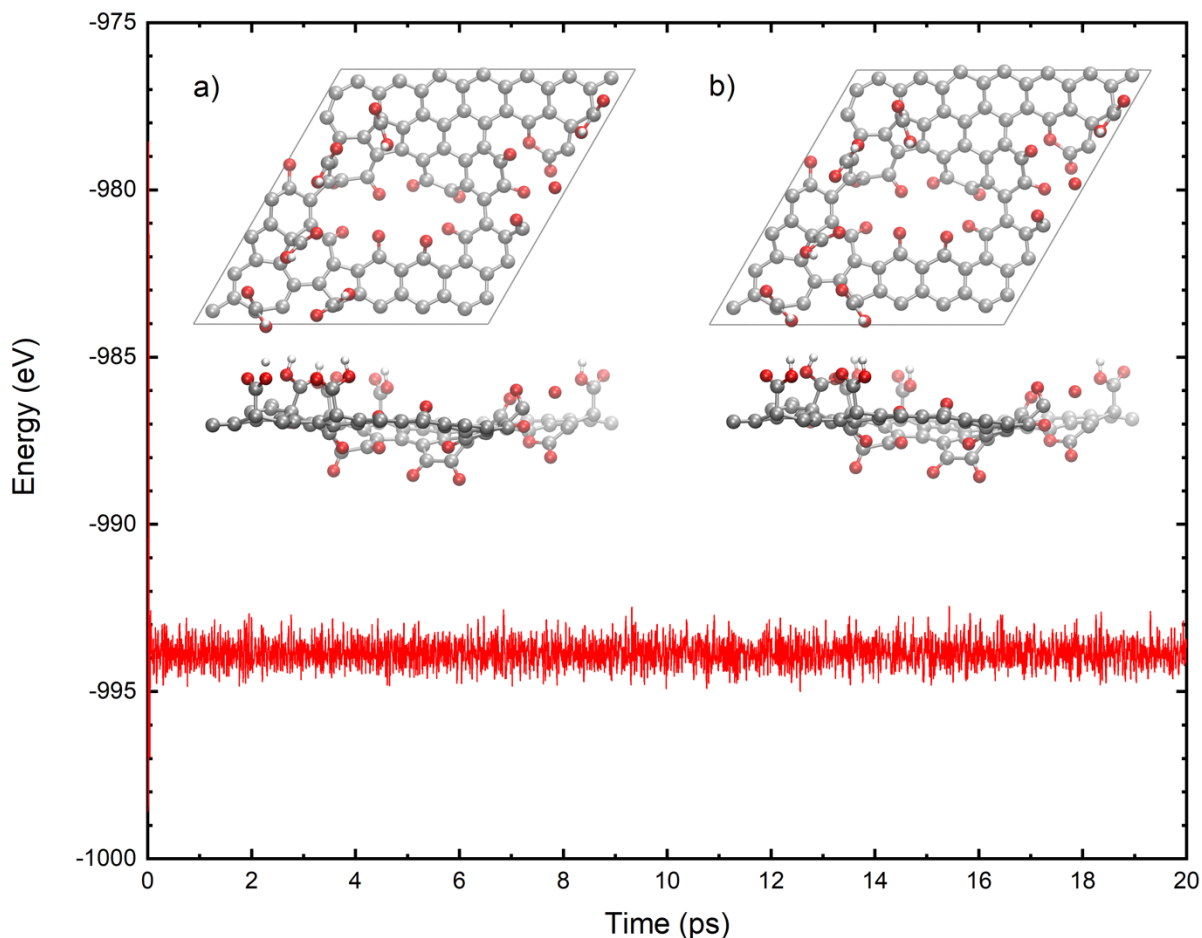


**Figure 3.** AIMD of the  $G_{ox}$  support, with the corresponding top and side views of initial (a) and final (b) structures shown as insets.

between layers and the lifting of some OFG that pointed towards the nearest graphene layer. Therefore, the single layer model appears to be a realistic model of carbon material as a support.

*Thermal stability.* The thermal stability of the optimized O-functionalized graphene ( $G_{ox}$ ) was investigated through an AIMD simulation at a temperature of 298 K, which can guide the design of carbon support with higher stability. With the initial geometry of the last relaxed structure, the simulation analysis revealed a very fast energy convergence over time, as shown in Figure 3. The final geometry of the simulation after relaxation (top and side views, right inset, Figure 3b) is very similar to the geometry of the starting point and the observed structural changes

are small, essentially rotations of carboxylic groups and out-of-plane deformations in the graphitic region, suggesting that at room temperature the designed  $G_{ox}$  support is stable.

**Characterization of the support.** Support characterization plays an important role in the process of catalyst design, and many techniques are now available for a complete characterization of the structure. To evaluate the validity of the computational model, analysis of the electronic and vibrational structure has been performed for both G and  $G_{ox}$ . The electronic behavior of graphene can be clearly seen in Figure 4a. Around the Fermi energy, pDOS exhibited a bandgap energy close to zero, characteristic of gapless semimetals. In contrast,  $G_{ox}$  differed from this behavior and presented a metallic character, as shown in Figure 4b, since it has a conduction band that is partially filled. The electronic band structure of these type of materials is not yet clearly understood due to nanoscale inhomogeneities in the structure, but optical studies indicate that it can be tuned by controlling the degree of functionalization.<sup>45,46</sup> On the other hand, more details can be obtained by analyzing the COHP function,<sup>33</sup> which provides an energy-based conception of chemical bonding. The COHP( $\epsilon$ ) profiles for the nearest-neighbor contacts in graphene and  $G_{ox}$  are also plotted in Figure 4a and Figure 4b, respectively. The predominant interactions of both graphene correspond to C–C interactions, which showed a bonding character of the states lying up to the Fermi level ( $\pi$  molecular orbitals, MO), followed by an antibonding character of the conduction states ( $\pi^*$  MO). However, in the case of  $G_{ox}$ , antibonding states appeared even below the Fermi level, around -6 eV, mainly due to C–O interactions. The IpCOHP, a bond strength index, is 10 eV per C–C interaction in the case of pristine graphene, and 7–12, 11–17, and 8 eV per C–C, C–O, and O–H interaction, respectively, in the case of  $G_{ox}$ .

The calculation of effective atomic charges plays an important role in understanding the electrostatic interactions that are established in a system. By Mulliken population analysis obtained by integrating the pDOS, the corresponding pMPA charges can be plotted. A representation of the

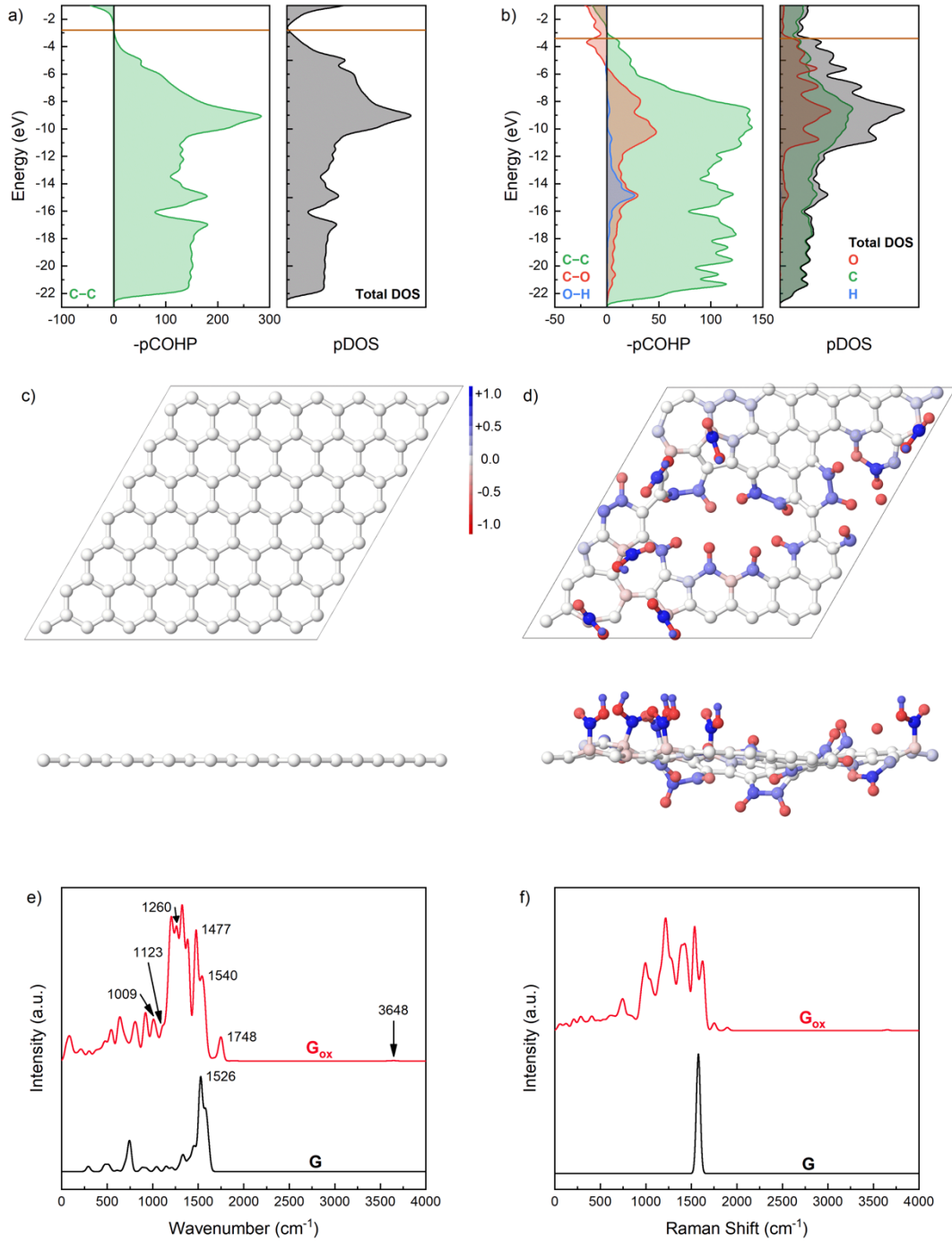


**Figure 4.** Characterization of graphene and  $G_{ox}$ . (a and b) Projected DOS and COHP profiles for the nearest-neighbor interactions. The position of the Fermi level (brown horizontal line) is also reported. pCOHP plots are calculated for nearest neighbors only. (c and d) Top and side views of projected MPA atomic charges. (e and f) Simulated IR and Raman spectra.

charge distribution in both materials is found in Figure 4. While pristine G (Figure 4c) clearly exhibits no electronic variation between all carbon atoms,  $G_{ox}$  (Figure 4d) expressed a wide variety

of charge ranging from positively charged in the case of carbon and hydrogen atoms attached to oxygen atoms, to negatively charged in the case of the oxygen atoms. This range of electrostatic interactions concentrated under the same material certainly opens up the possibility of using  $G_{ox}$  in electron exchange applications.<sup>15</sup>

Furthermore, the identification of the OFG and the chemical composition in the  $G_{ox}$  material is corroborated by means of IR (Figure 4e) and Raman (Figure 4f) spectroscopy. The IR spectrum of G mainly presented a single intense band at  $1526\text{ cm}^{-1}$  (stretching of C=C aromatic bonds), while  $G_{ox}$  presented a more complex IR spectrum. A detailed analysis on the vibrational modes of the most significant IR bands is collected in Table 1. The typical broad band between  $2400\text{-}3400\text{ cm}^{-1}$  associated to the stretching vibration of O–H groups is not present in the oxidized material. Two explanations appear as plausible for this mode to appear inactive: the absence of solvent and, therefore, of possible H bonds with the acid group that highlight the IR signal, or the harmonic approximation used to determine the vibrational frequencies, since the presence of light atoms such as hydrogen causes the incorporation of anharmonic corrections to be almost essential for a proper description. The bands located at  $1750$  and  $1540\text{ cm}^{-1}$  have been assigned to stretching vibration of C=O carboxyl/lactone and carbonyl groups, respectively. Compared with G spectrum, the aromatic C=C band showed a red-shift centered at around  $1480\text{ cm}^{-1}$ .

Finally, the presence of C–O bonds is confirmed, and the corresponding IR bands can be observed at around  $1260$ ,  $1120$  and  $1010\text{ cm}^{-1}$ , which have been assigned to vibrations from ether, carboxyl and lactone functional groups, respectively. In overall, simulated IR spectra reproduced rather well the characteristic IR band positions previously assigned in the literature<sup>47,48</sup> and the ones obtained for  $CNT_{ox}$  (see Figure S4). It should be noted that, while the O–H hydroxyl band appeared at relatively lower values, both the C=O carbonyl and C=C aromatic bands appeared at

**Table 1.** Obtained IR bands (in  $\text{cm}^{-1}$ ) from the simulated spectrum of  $G_{\text{ox}}$ ,<sup>a</sup> assignment of the vibration mode of the different functional groups, and experimental IR frequencies for the  $\text{CNT}_{\text{ox}}$  support.<sup>b</sup>

IR band	Vibrational mode	Functional group	$\text{CNT}_{\text{ox}}$
3648	$\nu(\text{O-H})$	Carboxyl	3260
1748	$\nu(\text{C=O})$	Lactone	–
	$\nu(\text{C=O})$	Carboxyl	1724
1540	$\nu(\text{C=O})$	Carbonyl	1680
1477	$\nu(\text{C=C})$	Aromatic	1568
1260	$\nu(\text{C-O})_{[\text{acyl}]}$	Lactone	
	$\nu(\text{C-O})$	Ether	
1123	$\nu(\text{C-O})$	Carboxyl	1180
	$\nu(\text{C-O})$	Ether	
1009	$\nu(\text{C-O})_{[\text{alkoxy}]}$	Lactone	

<sup>a</sup>IR bands refer to those bands shown in Figure 4c.

<sup>b</sup>See Figure S4 for the IR spectrum.

slightly higher values, in this case the  $\text{C=O}$  from carboxyl and globally all the  $\text{C-O}$  bands of the OFG agreeing relatively better.

The Raman spectrum of G (Figure 4f) displayed no disorder-induced D-band, as no defects are present, and a narrow G-band originated from the bond stretching of  $sp^2$  atoms at  $1577 \text{ cm}^{-1}$ , in line with the value of  $1585 \text{ cm}^{-1}$  from experiments in single graphene sheets,<sup>49</sup> and  $1580 \text{ cm}^{-1}$  in FLG (Figure S5). Importantly, the inclusion of OFG ( $G_{\text{ox}}$  in Figure 4f) caused a broadening of the G-band, leading to a series of new high-intensity bands red-shifted with respect to the G-band of pristine graphene, located in a range similar to the broad D-band in the experimental data (around

1300  $\text{cm}^{-1}$ ). Nonetheless, due to the closeness in the frequencies of the  $sp^3$  carbon Raman-active band ( $-\text{COOH}$  moieties attached to graphitic areas) and the D-band of graphitic carbons, both types of bands could merge under the same broad spectral feature. Lastly, in structures with well-defined double bonds, active blue-shifted Raman bands can be detected, although their intensity is usually low.<sup>50</sup> In the case of  $\text{G}_{\text{ox}}$ , there are two Raman peaks above the G-band of graphene, one of higher intensity at 1623  $\text{cm}^{-1}$ , and the other at 1752  $\text{cm}^{-1}$ . After inspecting the atoms involved in these normal modes, these vibrations come from the displacements of the carbon atoms in five- and seven-membered rings simultaneously, as a consequence of the reconstructed DV. Therefore, the defects can also induce blue shifts. Such spectrum modifications are not visible in the case of  $\text{FLG}_{\text{ox}}$  or  $\text{CNT}_{\text{ox}}$  (see Figure S5), probably because of the large number of graphene layers (around 10) in these materials.

**Anchorage of  $\text{Pd}_{\text{SA}}$  and of  $\text{Pd}_{13}$  cluster.** Once the pristine graphene has been functionalized, it can be used as support for metal deposition. In the case of Pd/C catalysts, it has been shown that both  $\text{Pd}_{\text{NP}}$  and  $\text{Pd}_{\text{SA}}$  can coexist on different types of carbon materials. Thus, mixtures of  $\text{Pd}_{\text{NP}}$  and  $\text{Pd}_{\text{SA}}$  were observed in commercial Pd/C catalysts prepared on activated carbon,<sup>18</sup> but also for Pd/CNT and Pd/FLG catalysts,<sup>51</sup> as revealed in **Erreur ! Source du renvoi introuvable.** The surface oxygen contents determined by XPS for the  $\text{CNT}_{\text{ox}}$  and  $\text{FLG}_{\text{ox}}$  supports used for Pd deposition were 5.7 and 3.8 at. %, respectively.<sup>52</sup> The Pd particle size distributions (particle size distribution based on total particles and on total atoms) of these three catalysts are given in Figure S6. The mean  $\text{Pd}_{\text{NP}}$  size in these samples varies between 0.9 (Pd/CNT) and 2.1 nm (Pd/FLG), and the percentage of  $\text{Pd}_{\text{SA}}$  between 48% (Pd/CNT) and 1.8% (Pd/FLG).

For the model catalyst, the inclusion of first a  $\text{Pd}_{\text{SA}}$  and then a small  $\text{Pd}_{\text{NP}}$  (*i.e.*, less than 1 nm, similar to the ones experimentally observed particularly in the Pd/CNT sample) was carried

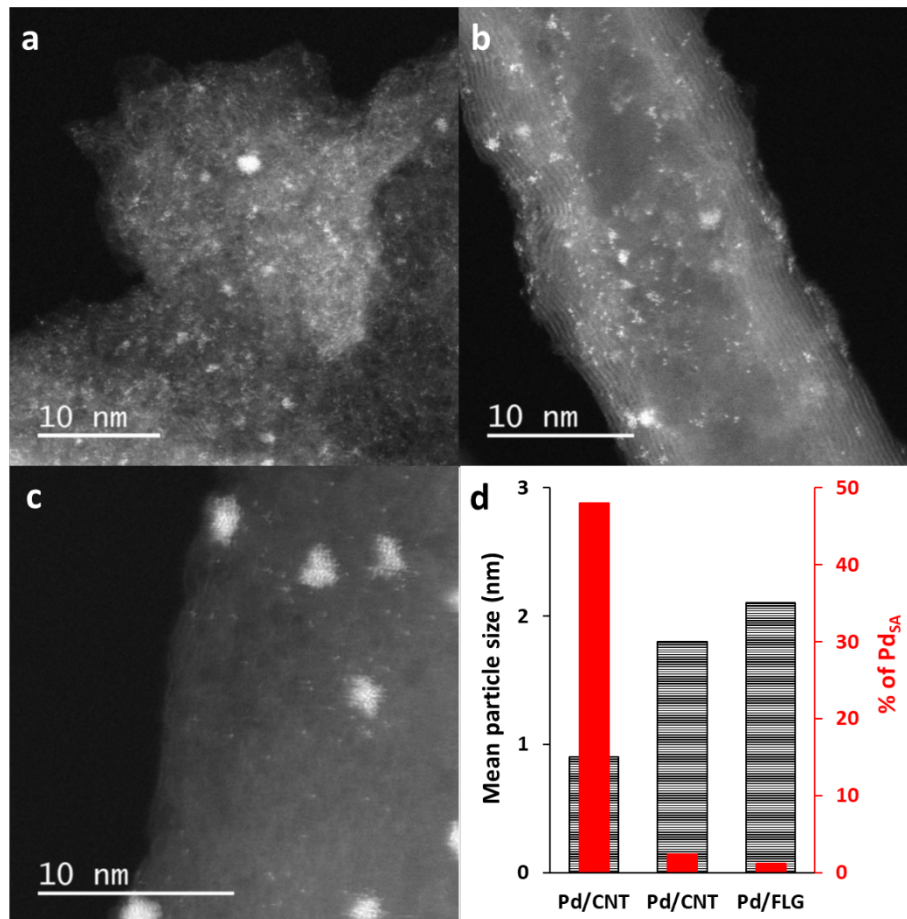


**Figure 5.** STEM-HAADF micrographs showing mixtures of Pd<sub>NP</sub> and Pd<sub>SA</sub> in: (a) 5% Pd/C; (b) 1.2% Pd/CNT; and (c) 1.5% Pd/FLG catalysts. (d) Mean Pd<sub>NP</sub> size and % of Pd<sub>SA</sub> in the Pd/C, Pd/CNT, and Pd/FLG catalysts.

out, to finally encompass both species on the same support. As the atomic radii of transition metals are larger than the one of carbon, metal adatoms are generally located above the graphene plane, a phenomenon that is more pronounced on SV than on DV.<sup>39</sup> In this regard, DV are suitable for metal adatom adsorption, which leads to thermodynamically more favorable situations.<sup>53</sup> This greater structural stability makes them less reactive (since they are less exposed on the surface) than the SA stabilized by SV. Therefore, the Pd atom adsorbed on an SV of the G<sub>ox</sub> as single-atom catalyst (SAC) was chosen in this study, as can be seen in Figure 6a. The SAC is thus modelled by removing a carbon atom in the graphene lattice, and subsequently adsorbing a Pd atom. It is

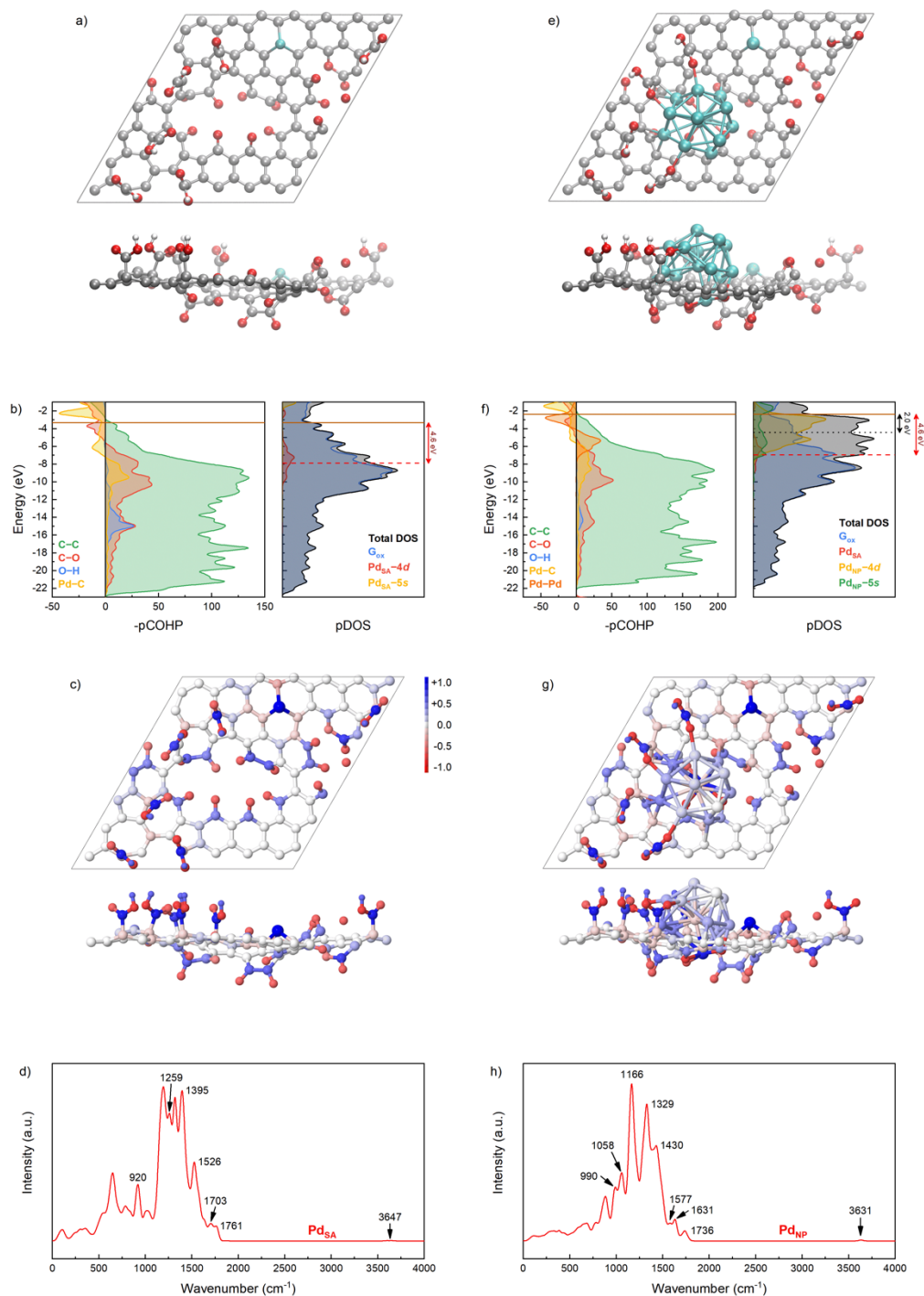


**Figure 6.** Characterization of anchored Pd<sub>SA</sub> and Pd<sub>SA</sub>+Pd<sub>NP</sub> catalysts. (a and e) Top and side views of atomistic structures. (b and f) Projected DOS and COHP profiles. (c and g) Top and side views of projected MPA atomic charges. (e and h) Simulated IR spectra. Conventions are the same as in Figure 4. The *d*-band center for SA (dashed red line) and NP (dotted black line) are also reported.

found that the vacancy formation energy on G<sub>ox</sub> is of about 5.6 eV, whereas according to the literature around 7.5 eV is needed to form a SV in graphene.<sup>54</sup> Thus, the removal of a carbon atom

from the graphene lattice appears to be slightly more favorable from a thermodynamic view-point in the case of  $G_{ox}$ . Different configurations were tested, the most stable being the one in which the carbon belonged to a six-membered ring of a graphitic region and far from any oxygen functionality. The metal anchored on support forms three covalent bonds with the neighboring carbons in a  $Pd-C_3$  coordination structure (average bond length of 1.95 Å) and is displaced outward by 1.01 Å from the graphitic surface, probably due to the intrinsic corrugation of the support itself.<sup>39</sup> The binding energy, calculated as the difference between the SAC and the energy of the SV oxygenated support plus the energy of the isolated Pd, is 4.1 eV, pointing towards a favorable energy process.

pDOS( $\epsilon$ ) and pCOHP( $\epsilon$ ) of  $Pd_{SA}$  are plotted in Figure 6b. Around the Fermi level, the total pDOS (in black) is still influenced by the  $G_{ox}$  (in blue), since the proportion of dispersed metal with respect to the support is very low. The Pd  $d$ -band center,  $\epsilon_d$ , calculated as the normalized, energy-weighted integral of the DOS, and projected onto all  $d$  AOs, is calculated to be 4.6 eV (in red on the pDOS plot). Whereas below the Fermi energy pCOHP (C–C and O–H,  $\epsilon$ ) are always positive, that of C–O showed a substantial back-donation in line with  $G_{ox}$ , so its origin must come from the  $\pi^*$  MO. In addition, the highest metal states have an antibonding Pd–C character. It was found that IpCOHP has exactly the same values per C–C, C–O, and O–H interactions as in the case of  $G_{ox}$ , while a value of 3 eV is taken for the newly formed Pd–C interactions. Furthermore, a change in the partial atomic charge of the Pd atom is observed by analyzing the electronic distribution. The electronic configuration of the ground state of gaseous neutral palladium is [Kr]  $4d^{10} 5s^0$ . However, when the metal is anchored to the SV, the computed average occupation of the bands became [Kr]  $4d^{8.8} 5s^{0.2}$ , undergoing an oxidation process (giving an electron to the carbon support) that makes it formally have an atomic charge of +1, corroborated by the intense blue color

in the corresponding pMPA charges of SAC depicted in Figure 6c. This presents the possibility of addressing a Pd<sup>+</sup>-based chemical reactivity. In the particular case of alkene hydrogenation reactions, having a Pd<sup>+</sup> can strengthen the Pd-alkene interaction resulting in less active catalysts.<sup>55</sup> Experimentally, it was shown that the X-ray Adsorption Near Edge Structure (XANES) spectrum of Pd<sub>SA</sub>/graphene is close to those of PdO, which implies that the Pd<sub>SA</sub> on graphene surface were mostly present in a +2-valence state.<sup>55</sup> In that case, the first shell peak for Pd<sub>SA</sub>/graphene was contributed to a mixture of Pd–O and Pd–C coordination.

As expected, the SAC IR profile is very similar to that of the support (represented in Figure 6d, for a detailed analysis on the assignment of the IR spectrum of the SAC see Table S2). The changes appear in the regions associated with the metal atom. Because of the presence of the newly formed Pd–C bonds, a new band assigned to the  $\nu(\text{Pd-C})$  appeared; in particular, the band around 920 cm<sup>-1</sup>. Pd<sub>SA</sub> anchoring caused the IR band corresponding to  $\nu(\text{C=C})$  to be displaced towards smaller values, going from 1477 to 1395 cm<sup>-1</sup>. In view of these results, IR spectroscopy can be considered as a useful technique for the study and identification of metal-carbon bonds during the preparation of SAC.

Regarding the Pd<sub>NP</sub>, a cluster model of 13 atoms is considered, which has been proven to be robust and enough efficient for describing theoretically the hydrogenation of alkenes.<sup>51</sup> Such clusters (according to their size) are representative of highly dispersed palladium catalysts (see **Erreur ! Source du renvoi introuvable.** and Figure S6 for Pd/CNT catalyst. For this, an isolated Pd<sub>13</sub> cluster according to geometric shell model was first optimized, obtaining a classical symmetric icosahedral (*I<sub>h</sub>*) structure. It was then deposited on the surface containing the Pd<sub>SA</sub>, optimizing the entire supported catalyst, the final structure of which can be found in Figure 6e. As it can be seen, the anchoring of the cluster took place in the carbonyl-decorated multiple vacancy.

In addition, twelve of the thirteen Pd atoms are accessible, so the theoretical metal dispersion is close to 100%. One of the main reasons is that the cluster is located at a reasonable distance from the Pd<sub>SA</sub>, minimizing the interaction, and thus preventing the agglomeration of the latter (the shortest distance between a Pd atom on the surface of the cluster and the Pd<sub>SA</sub> is greater than 5 Å). The Pd<sub>SA</sub> maintained the same structural properties (average Pd–C bond length of 1.96 Å and elevation height of 1.02 Å) as before anchoring the cluster, which endorses the weak interaction between both species. Moreover, a very strong interaction (adsorption energy of 8.8 eV) is denoted between the Pd<sub>13</sub> cluster and the support, in agreement with the values reported in the literature for the same cluster size.<sup>56</sup> The size of the vacancy is of paramount importance to accommodate and tightly binding the metal clusters, as large vacancy defect sites allow the formation of multiple Pd–C bonds that increase the binding. This inevitably leads to a final cluster slightly distorted compared to the initial icosahedral structure, where the Pd–C bonds are in the range between 2.1 and 2.7 Å, and those of Pd–O between 2.0 and 2.3 Å. For all these reasons, the DV motif turns out to be another way to prevent the progressive leaching of the cluster during catalysis.

Through the structure-property analysis of the supported cluster, few meaningful structural parameters are investigated. For example, making use of the nearest neighbor search, the average first nearest-neighbor (NN) Pd–Pd bond length (R) is of 2.62 Å, significantly shorter than the distance obtained by EXAFS for Pd/C catalysts with larger NP size (around 2.74 Å).<sup>57,58</sup> The average NN Pd–Pd coordination number (CN) is of 4.92, although with clearly different values in the case of the Pd atom located in the core of the cluster (CN = 10) and those located on the surface (CN = 4.50). Additionally, the mean interatomic distance (MIAD) was calculated, which reflects the effective radius of a cluster and allows, for example, an analysis of morphological change.<sup>59</sup> In this case, MIAD had a value of 3.77 Å. These numbers are in excellent agreement with those of

isolated Pd<sub>13</sub> reported in the literature,<sup>60</sup> with R = 2.64 Å, CN = 6.46, and MIAD = 3.62 Å, highlighting that the fact of being supported caused no excessive structural change, only a relative decrease in the CN mainly due to a partial cluster opening on the face closest to the support. To provide a more precise information on the structure of the cluster during the adsorption process, the pair distribution functions of both the isolated and anchored species were analyzed (see Pd<sub>13</sub> black and Pd<sub>13</sub>@G<sub>ox</sub> blue curves of Figure S7, respectively). While the peaks in both situations appeared at approximately the same Pd–Pd bond lengths, there is an increase in metallic interactions at higher distances in the case of the anchored Pd<sub>13</sub>, which would explain the differences observed for the CN.

In Figure 6f, the pDOS( $\epsilon$ ) and pCOHP( $\epsilon$ ) of the Pd<sub>SA</sub> and Pd<sub>NP</sub> species are shown. Contrary to what happens in Pd<sub>SA</sub>, a greater contribution by metal atoms in the electronic states around the Fermi energy is observed. In this case, the metallic character of the cluster can be clearly appreciated, mainly by the Pd *d* component (in yellow) towards values below the Fermi level and by the Pd *s* component (in green) at values above the Fermi energy. The Pd *d*-band center for both the cluster (dashed red line) and the single atom (dotted black line) anchored on the support is calculated to be 2.0 and 4.6 eV, respectively. In the case of the former, the *d*-band center stabilizes 0.3 eV with respect to the bare cluster by means of bonding interactions with surface C atoms, widening the *d* band. On the other hand, with an identical value of  $\epsilon_d$  for Pd<sub>SA</sub>, the presence of Pd<sub>13</sub> has scarcely influenced the local electronic structure of the Pd<sub>SA</sub>. Regarding the pCOHP plot, the presence of bonding states between -8 and -4 eV and antibonding states between -4 and -1 eV with respect to Pd<sub>SA</sub> is remarkable, related to the deposition of the Pd<sub>13</sub> cluster. The highest occupied states are essentially established on metal atoms (Pd–Pd interactions), exhibiting an antibonding character (negative values of -pCOHP). The latter specifically bears similarity to the electronic

structure of small organometallic clusters.<sup>61</sup> The bond strength index IpCOHP is found to be 0.9 eV per Pd–Pd interaction, somewhat higher than the value of 0.7 eV obtained for the isolated non-anchored cluster, which suggests a metal-metal strengthening by the Pd<sub>13</sub> deposition on G<sub>ox</sub>.

An important change can also be deduced in the electronic distribution of the cluster, in line with what is observed when the Pd<sub>SA</sub> is anchored. The mean valence electron occupation of each of the palladium atoms is 4d<sup>9.2</sup> 5s<sup>0.6</sup>, so taking into account the 13 atoms there is a total difference of three electrons less with respect to the expected value. This means that apparently the cluster is formally [Pd<sub>13</sub>]<sup>3+</sup>. However, among all the Pd atoms of the cluster, the one located at the base had a lower electronic occupation than the rest, reminiscent of a Pd<sup>2+</sup> in a square-planar environment according to the optimized geometry, so formally the cluster is more close to [(Pd<sub>1</sub>)<sup>2+</sup>(Pd<sub>12</sub>)<sup>+</sup>]. G<sub>ox</sub> is then acting as an electron acceptor when it is in direct contact with a metal such as palladium, regardless of whether it is presented as SA or ultra-small NP, which is in agreement, according to the work function of both the metal and carbon or oxygen from the support. This outcome can also be confirmed together with the charge density map in Figure 6g. Clearly, Pd<sub>SA</sub> continued to have a very positive charge density, while Pd<sub>13</sub> offered a wide range of densities.

Finally, the IR spectrum with both forms of metallic species is shown in Figure 6h. The clearest evidence that would reveal the presence of the Pd<sub>13</sub> cluster corresponds to  $\nu(\text{Pd-Pd})$ , but unfortunately, they appear at frequencies below 300 cm<sup>-1</sup>, characteristic of the fingerprint region, often the most complex and confusing region to interpret. However, other evidence in more favorable regions is observed, as is the case of the  $\nu(\text{C=O})$  of carbonyl groups sharing electronic density with Pd<sub>13</sub> atoms. For example, C=O stretching vibration of carboxylic acid groups in G<sub>ox</sub> usually appear in a range of about 1710 and 1740 cm<sup>-1</sup>, but when they are coordinating to an atom

of the metal cluster a significant red-shift is denoted, in this case between 1560 and 1630  $\text{cm}^{-1}$ . Similar behavior with the stretching vibration of ketone (and quinone) groups is appreciated, since in their free coordination state they appear between 1620 and 1680  $\text{cm}^{-1}$  (1640 and 1700  $\text{cm}^{-1}$  for quinone), and when coordinated to a Pd atom the peak is red-shifted to values of about 1230 and 1410  $\text{cm}^{-1}$  (approx. 1320  $\text{cm}^{-1}$  for quinone). Therefore, while direct measurements of metal-metal bonds are difficult to characterize by IR spectroscopy, indirect measurements such as surface adsorbates coordinated to metal appear as a plausible solution.

**Cluster hydrogenation.** Supported Pd catalysts are attractive for hydrogenation reactions, since palladium is considered the most selective among Group 10 metals. High dispersion is a prime asset of these catalysts, where the small metal NP have the ability to be hydrogenated. This also results in an important class of materials with significant potential for energy storage and energy-related applications.<sup>62</sup> By means of a systematic analysis, the hydrogenation of the supported Pd<sub>13</sub> cluster is evaluated on the G<sub>ox</sub>. Since H<sub>2</sub> dissociates easily at the cluster surface, it is basically covered with surface hydrides. According to what has been previously reported for hydride Ru<sub>NP</sub>,<sup>63,64</sup> a hydrogen to metal ratio (H/M)<sub>NP</sub> of approximately 1.5/1 has been used to ensure complete saturation, so the final stoichiometry turned out to be Pd<sub>13</sub>H<sub>20</sub>, as illustrated in Figure 7a. It is important to highlight the outcropping towards the surface that metal cluster experienced with respect to the situation prior to hydrogenation, where the binding to the support was very noticeable. Even so, this prominent elevation has already been observed for  $\gamma$ -alumina-supported Pt nanoparticles.<sup>65</sup> The metallic cluster went from being anchored by means of a square planar molecular geometry formed by four carbonyl groups, in addition to numerous interactions between the rest of Pd atoms and graphene carbons, to being anchored by only two CO groups and three H atoms. This could cause potential stability problems under H<sub>2</sub> environments as is often observed

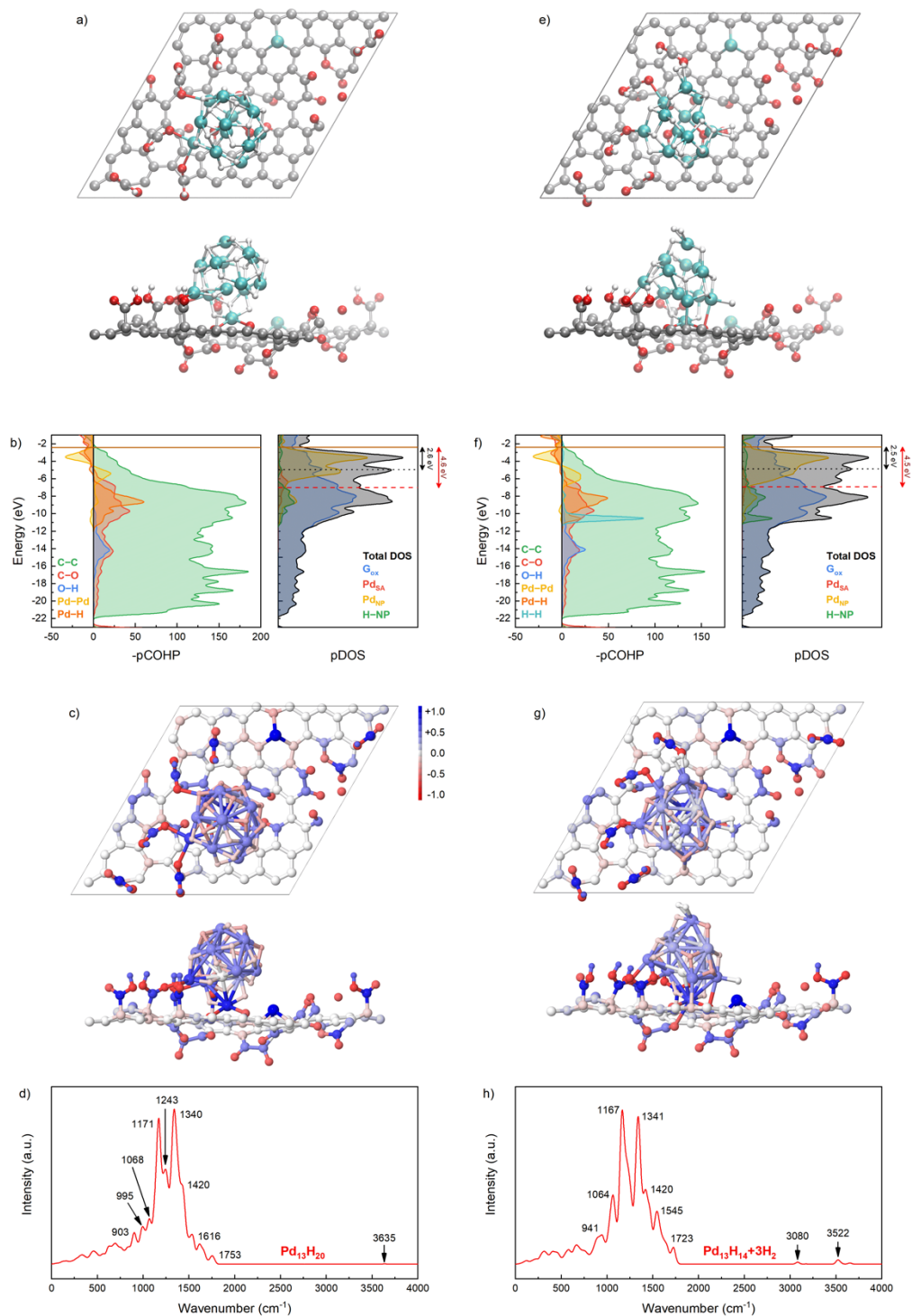


**Figure 7.** Characterization of hydrogenated  $\text{Pd}_{13}\text{H}_{20}$  and  $\text{Pd}_{13}\text{H}_{14}+3\text{H}_2$  catalysts. **(a and e)** Top and side views of atomistic structures. **(b and f)** Projected DOS and COHP profiles. **(c and g)** Top and side views of projected MPA atomic charges. **(d and h)** Simulated IR spectra. Conventions are the same as in Figure 4 and Figure 6.

for  $\text{Pd}_{\text{NP}}$ ,<sup>66</sup> resulting in sintering of the metal, although in general it occurs at relatively elevated temperatures. The  $\text{Pd}_{\text{SA}}$  is not affected by the hydrogenation process, with an elevation height of

1.00 Å in line with the previous values. Regarding the nature of hydrogen atoms, they sit in high coordination sites, showing preference for hollow adsorption sites (coordinated to three Pd atoms), and to a lesser extent for the bridge ones (coordinated to two Pd atoms), revealing no hydrogen adsorption at top sites (coordinated to a single Pd atom), as occurs on extended Pd surfaces.<sup>67</sup> Since the twenty H atoms can be interpreted as ten fully dissociated H<sub>2</sub> molecules, the hydrogenation energy of Pd<sub>13</sub> can be calculated as the difference between Pd<sub>13</sub>H<sub>20</sub> and the energy of Pd<sub>13</sub> plus the energy of ten H<sub>2</sub>, obtaining a favorable value of -4.6 eV. On the other hand, the adsorption energy directly from the hydrogenated cluster can also be calculated, and it is found to be -4.2 eV, so from an anchoring point of view, the process appears to be less thermodynamically favorable compared to the bare cluster. A structural analysis of the cluster using the NN algorithm revealed an average Pd–Pd bond length and an effective radius of 2.74 and 3.95 Å; around 0.1 and 0.2 Å higher, respectively compared to the non-hydrogenated situation, showing a generalized swelling. The average Pd–H bond length is found to be 1.75 Å, and the mean Pd–Pd and Pd–H coordination number is 4.92 and 2.75 respectively, a value in the case of the former CN identical to the bare cluster. Therefore, there has not been a loss of local coordination of Pd atoms by the dissociative adsorption of the H<sub>2</sub> molecules. Considering the pair distribution function of the hydrogenated cluster (see Pd<sub>13</sub>H<sub>20</sub>@G<sub>ox</sub> red curve in Figure S7), the appearance of a small intensity peak around 3.65 Å (almost 1 Å larger than the main peak) would also explain the slight increase in observed size. Furthermore, the hydrogenation of the anchored Pd<sub>SA</sub> is also evaluated in the G<sub>ox</sub>. According to the calculations, H<sub>2</sub> can be easily adsorbed on the metal center with an adsorption energy around 0.4 eV. However, both homolytic and heterolytic H<sub>2</sub> activation is clearly endothermic (reaction energies greater than 0.4 eV relative to bare G<sub>ox</sub>), so it will not take place. It appears, therefore,

that the only plausible way to have an H atom on Pd<sub>SA</sub> forming the Pd<sub>SA</sub>-H species is through an H-spillover mechanism.

The corresponding pDOS and pCOHP plots are represented in Figure 7b. The presence of hydrogen atoms in the Pd cluster caused the total pDOS to be dominated with less intensity by the metal in the states around the Fermi level compared to the situation prior to hydrogenation. The *d*-band center for both the Pd<sub>NP</sub> and the Pd<sub>SA</sub> is calculated to be 2.6 and 4.5 eV, slightly higher for the case of the former, and exactly the same for the case of the latter compared to the pre-hydrogenated situation. This stabilization in the metallic cluster was also computationally observed for ruthenium NP.<sup>68</sup> It is worth highlighting the appearance of states around -9 eV corresponding to the new H atoms, clearly differentiated from the ones belonging to the carboxylic acid groups, located around -15 eV. Below the Fermi level, a subtly more accentuated antibonding character than in the case of the bare Pd<sub>13</sub> cluster is revealed from the pCOHP plot for the highest Pd states, which further weakens the metal-metal bond, going from an IpCOHP index of 0.9 to only 0.4 eV per intermetallic interaction. However, a value of 2 eV is calculated for the newly exposed metal-H interaction. These results provided evidence on the existing polarization in the new hydrogenated clusters, as pointed out by the pMPA maps in Figure 7c. Comparing both bare and hydrogenated metallic NP, a clear tendency to oxidation of the palladium atoms is observed, turning an increasingly intense blue color in the case of the surface atoms and a whitish color in the case of the core atom (it should be noted that the core atom had a slightly negative atomic charge). Instead, hydrogen atoms could be considered as hydrides, as indicated by their reddish colorations. A more in-depth analysis on the electronic structure of the cluster was carried out to elucidate the charge balance between metals and adsorbates. Because the metal is in a low oxidation state (it is originally a *d*<sup>10</sup>, so rich in electrons) and the hydrogen adsorbate possesses

low-lying empty orbitals, then a metal-to-adsorbate charge transfer transition may occur. Specifically, up to four and one electron were transferred to the hydrogen adsorbates and also to  $G_{ox}$ , respectively, so finally the charge balance elucidated a  $[Pd_{13}H_{20}]^+$  cluster.

The simulated IR spectrum is depicted in Figure 7d. The most outstanding difference compared to the spectrum of the bare cluster appeared around 1171 and 1340  $cm^{-1}$ , corresponding to the  $\nu(Pd-H)$  stretching vibrations. The normal modes of the metal–hydrogen interactions were observed in a wide range of frequencies due to the heterogeneity of palladium and hydrogen atoms forming the metallic nanostructure, ranging from 1100 to 1450  $cm^{-1}$ . Therefore, the IR bands at 1243 and 1420  $cm^{-1}$ , related to the  $\nu(C-O)$  of lactone and ether functional groups, and  $\nu(C=C)$  of aromatic carbons, respectively, could have experienced a relative increase in intensity. A decay of the infrared intensity appearing at 995  $cm^{-1}$ , assigned to the  $\nu(Pd-C)$  stretching mode, can also be detected mainly as a consequence of the elevation experienced by the  $Pd_{13}H_{20}$  cluster, and therefore the gradual disappearance of metal–carbon interactions.

*Thermal stability.* The thermal stability of the supported metal catalyst is also evaluated by means of a MD simulation at room temperature, in a procedure analogous to that carried out for the  $G_{ox}$  support (the evolution of the energy of the system over the simulation time can be found in Figure S8). As expected, the data analysis of the simulation trajectory mostly revealed changes in the cluster region, which underwent a gradual deformation, inevitably leading to a non-reversible process. Although it maintained the distorted icosahedron shape as shown in Figure 7e, it is interesting to note the creation of local octahedra that were previously unappreciated. The most striking feature of this Pd atom rearrangement is the hydrogen recombination on the surface of the cluster, probably due to the high coverage of H atoms originally introduced. The appearance of dihydrogen took place from the first picoseconds of simulation, after which up to three new

molecules appeared. Once formed, the H<sub>2</sub> molecules remained coordinated at the Pd<sub>13</sub> surface, suggesting a higher H<sub>2</sub> adsorption energy than the thermal energy to desorb. This resulted in a stoichiometry of Pd<sub>13</sub>H<sub>14</sub>(H<sub>2</sub>)<sub>3</sub>, decreasing the effective H/M ratio to practically unity. Dihydrogen complexes M( $\eta^2$ -H-H) are notable in palladium chemistry, definitely acting as  $\sigma$  complexes in reaction intermediates.<sup>69</sup>

Taking a more detailed analysis of the structure-property of the renewed catalyst, the energy difference between the supported structures Pd<sub>13</sub>H<sub>20</sub> and Pd<sub>13</sub>H<sub>14</sub>+3H<sub>2</sub> is calculated to be -1.3 eV, so clearly the system obtained after thermal equilibration was more stable. To ensure if the energy variation came mainly from the structural reorganization of the cluster framework or from the new arrangement of the H atoms, again parameters such as average bond length, mean CN, and MIAD were calculated. For the Pd<sub>13</sub>H<sub>14</sub>+3H<sub>2</sub> species, the intermetallic and metal-H distances, as well as the MIAD, were 2.66, 1.73, and 3.92 Å, respectively; all values very close to those calculated for the fully hydrogenated species. In fact, the Pd-Pd distance returned to the same value as the isolated gas-phase cluster (around 2.64 Å). Coordination numbers were the ones that caused the most difference: around 4.31 (CN<sub>Pd-Pd</sub>) and 2.05 (CN<sub>Pd-H</sub>) compared to 4.92 and 2.75 in the case of the Pd<sub>13</sub>H<sub>20</sub> stoichiometry. This decrease was probably caused by the local opening of the bottom of the metallic structure, causing a Pd-C interaction to compensate for the loss of coordination. The pair distribution function of the thermalized cluster (see Pd<sub>13</sub>H<sub>14</sub>+3H<sub>2</sub>@G<sub>ox</sub> green curve in Figure S7) revealed a significant reduction in the number of closest metallic interactions (peak around 2.65 Å), and the appearance of a small peak at Pd-Pd bond lengths of approximately 6.5 Å, which would explain the decrease in intermetallic coordination observed. For all this, the stability achieved by the combined H/H<sub>2</sub> species is largely driven by the rearrangement of the

hydrogen atoms, contributing to a lesser tendency towards sintering processes, operating at elevated temperatures in hydrogen-rich atmospheres.

Since the composition of these species is essentially the same, subtle changes in the electronic structure are appreciated. As the pDOS and pCOHP plots of Figure 7f pointed out, the emergence of states between -11 and -10 eV (always positive below the Fermi energy) is the most relevant difference compared to Pd<sub>13</sub>H<sub>20</sub>, belonging to the H<sub>2</sub> coordination (light blue curve in the pCOHP plot). These results give an interesting indication that co-adsorbed species capable of mobilizing *d* AOs from the Pd cluster surface could favor sideway H<sub>2</sub> coordination. Regarding the pMPA charges represented in Figure 7g, a general withdrawal of the positive electron density of the Pd cluster atoms is appreciated, promoted by the migration of hydrogen atoms (*i.e.*, by the negative charge density migration due to partial hydride character) during recombination into molecular hydrogen. In turn, the latter all elucidated a symmetry in the electric charge of the H–H bond, expressing a dominant homolytic component.

Finally, in Figure 7h the simulated IR spectrum of Pd<sub>13</sub>H<sub>14</sub>+3H<sub>2</sub> is represented. Due to the recombination of some H atoms into molecular hydrogen, a small peak at 3080 cm<sup>-1</sup> corresponding to  $\nu(\text{H-H})$  is originated. It is experimentally observed that the H–H stretching mode for the side-bonded Pd(H<sub>2</sub>) complex occurs at 2971 cm<sup>-1</sup> with a very low relative integrated intensity,<sup>70</sup> consistent with what has been computationally observed so far, the small differences probably coming from the size of the metallic entity. As a consequence of the new metal–dihydrogen interaction, the corresponding  $\nu(\text{Pd-H}_2)$  vibrational mode is perceived at frequencies significantly higher than those of Pd–H<sup>δ-</sup> band. Specifically, it can be found from 1450 to 1650 cm<sup>-1</sup>, being extended the entire band in values between 1100 and 1650 cm<sup>-1</sup>. Therefore, the appearance of

possible changes in the nature of the supported catalyst could be diagnosed via IR spectroscopy by comparing with the reported computational data.

#### 4. CONCLUSIONS

An O-functionalized graphene (carbon support) as well as supported Pd<sub>SA</sub> and Pd<sub>13</sub> nanocluster (supported metal catalysts) have been computationally modelled by means of periodic DFT simulations. Structure-property characteristics, as well as electronic properties and vibrational features have been analyzed in detail. For the functionalized carbon support, the inclusion of point defects and experimentally probed abundant OFG have been taken into account, demonstrating high thermal stability at room temperature. The characterization has confirmed the structural motifs introduced in the model, distinguishing the organic functionalities and the vacancy defect by IR and Raman spectroscopy, respectively; and showing the nature of the new interactions according to their electronic structure, which revealed a material of metallic character. On the other hand, the simultaneous inclusion of both classes of metallic species has been carried out in clearly differentiated regions of the support surface and directly on the defects to prevent processes such as agglomeration. It is important to highlight the red shift of the IR bands governed by interactions with the metal, in addition to a significant reduction in the electron density of the supported metal species. Finally, the nanocluster has been fully hydrogenated, as a relevant state in hydrogenation processes, being less exposed to the surface due to the absorbed hydrogen atoms. However, a second thermal equilibration of the system has shown the recombination of up to three H<sub>2</sub> molecules, specifying that the H/M ratio for the studied system is approximately unity.

#### ▪ ASSOCIATED CONTENT

#### **Supporting Information**

The Supporting Information is available free of charge at:  
<http://pubs.acs.org/doi/10.1021/acsanm.XXXXXXX>.

Experimental section; TPD/MS spectra of the CNT<sub>ox</sub> support (Figure S1); density of OFG measured on CNT and FLG (Figure S2); atomistic structure of rhombohedral (ABC stacking order) trilayer graphene (Figure S3); Fourier transform infrared spectra for CNT and CNT<sub>ox</sub> (Figure S4); Raman spectra of CNT, CNT<sub>ox</sub>, FLG, and FLG<sub>ox</sub> (Figure S5); particle size distribution based on total particles and on total atoms for 5% Pd/C, 1.2% Pd/CNT, and 1.5% Pd/FLG catalysts (Figure S6); Pd–Pd pair distribution functions for the obtained cluster structures (Figure S7); AIMD simulation of Pd<sub>SA</sub>+Pd<sub>13</sub>H<sub>20</sub> supported catalyst (Figure S8); results of the deconvolution of CO<sub>2</sub> and CO TPD spectra of CNT<sub>ox</sub> (Table S1); finally, the obtained IR bands from the simulated spectra of the different optimized structures (Table S2) (PDF).

#### ▪ AUTHOR INFORMATION

##### Corresponding Author

**Philippe Serp** – LCC–CNRS, Université de Toulouse, INPT, 205 Route de Narbonne, F-31077 Toulouse, Cedex 4, France; ORCID: [orcid.org/0000-0003-1424-2724](https://orcid.org/0000-0003-1424-2724); E-mail: [philippe.serp@ensiacet.fr](mailto:philippe.serp@ensiacet.fr)

**Iann C. Gerber** – LPCNO, Université de Toulouse, INSA–CNRS–UPS, 135 Avenue de Rangueil, F-31077 Toulouse, Cedex 4, France; ORCID: [orcid.org/0000-0001-5091-2655](https://orcid.org/0000-0001-5091-2655); E-mail: [igerber@insa-toulouse.fr](mailto:igerber@insa-toulouse.fr)

##### Authors

**Javier Navarro-Ruiz** – *LPCNO, Université de Toulouse, INSA–CNRS–UPS, 135 Avenue de Rangueil, F-31077 Toulouse, Cedex 4, France*; ORCID: [orcid.org/0000-0002-3604-9338](https://orcid.org/0000-0002-3604-9338)

**Camila Rivera-Cárcamo** – *LCC–CNRS, Université de Toulouse, INPT, 205 Route de Narbonne, F-31077 Toulouse, Cedex 4, France*; ORCID: [orcid.org/0000-0002-4398-2863](https://orcid.org/0000-0002-4398-2863)

**Bruno Machado** – *LSRE–LCM, Chemical Engineering Department, Faculty of Engineering, University of Porto, Rua Dr. Roberto Frias s/n, 4200-465 Porto, Portugal*; ORCID: [orcid.org/0000-0003-3183-7519](https://orcid.org/0000-0003-3183-7519)

**Iker del Rosal** – *LPCNO, Université de Toulouse, INSA–CNRS–UPS, 135 Avenue de Rangueil, F-31077 Toulouse, Cedex 4, France*; ORCID: [orcid.org/0000-0001-6898-4550](https://orcid.org/0000-0001-6898-4550)

Complete contact information is available at:

<http://pubs.acs.org/doi/10.1021/acsanm.XXXXXXX>.

## Notes

The authors declare no competing financial interest.

### ▪ ACKNOWLEDGMENTS

This work has received funding from the French Agence Nationale de la Recherche under grant agreement ANR-19-CE07-0030. J. N.-R., I. del R., and I. C. G. acknowledge the “Calcul en Midi-Pyrénées” initiative CALMIP (Projects p0812 and p1214) for the computer resources. The authors also thankfully acknowledge the HPC resources at CINES, IDRIS, and TGCC under the allocation 2021-A0100906649 made by GENCI.

## ▪ REFERENCES

- (1) Ma, Z.; Zaera, F. Heterogeneous Catalysis by Metals. In *Encyclopedia of Inorganic Chemistry*; King, R. B., Cabtree, R. H., Lukehart, C. M., Atwood, D. A., Scott, R. A., Eds.; John Wiley & Sons, Ltd, 2005.
- (2) *Applied Homogeneous Catalysis with Organometallic Compounds*, 3rd ed.; Cornils, B., Herrmann, W. A., Beller, M., Paciello, R., Eds.; WILEY-VCH Verlag: Weinheim, Germany, 2002; Vol. 1.
- (3) Rothenberg, G. Heterogeneous Catalysis. In *Catalysis*; WILEY-VCH Verlag: Weinheim, Germany, 2008; pp 127–187.
- (4) Xiong, M.; Gao, Z.; Qin, Y. Spillover in Heterogeneous Catalysis: New Insights and Opportunities. *ACS Catal.* **2021**, *11* (5), 3159–3172.
- (5) van Deelen, T. W.; Hernández Mejía, C.; de Jong, K. P. Control of Metal-Support Interactions in Heterogeneous Catalysts to Enhance Activity and Selectivity. *Nat. Catal.* **2019**, *2* (11), 955–970.
- (6) Gerber, I. C.; Serp, P. A Theory/Experience Description of Support Effects in Carbon-Supported Catalysts. *Chem. Rev.* **2020**, *120* (2), 1250–1349.
- (7) Serp, P. Carbon. In *Comprehensive Inorganic Chemistry II*; Reedijk, J., Poeppelmeier, K., Eds.; Elsevier: Amsterdam, 2013; pp 323–369.
- (8) Xi, J.; Yang, S.; Silvioli, L.; Cao, S.; Liu, P.; Chen, Q.; Zhao, Y.; Sun, H.; Hansen, J. N.; Haraldsted, J.-P. B.; Kibsgaard, J.; Rossmeisl, J.; Bals, S.; Wang, S.; Chorkendorff, I.

- Highly Active, Selective, and Stable Pd Single-Atom Catalyst Anchored on N-Doped Hollow Carbon Sphere for Electrochemical H<sub>2</sub>O<sub>2</sub> Synthesis Under Acidic Conditions. *J. Catal.* **2021**, *393*, 313–323.
- (9) Serp, P.; Machado, B. F. *Nanostructured Carbon Materials for Catalysis*; Catalysis Series; The Royal Society of Chemistry, 2015.
- (10) Machado, B. F.; Serp, P. Graphene-Based Materials for Catalysis. *Catal. Sci. Technol.* **2012**, *2* (1), 54–75.
- (11) Xi, J.; Jung, H. S.; Xu, Y.; Xiao, F.; Bae, J. W.; Wang, S. Synthesis Strategies, Catalytic Applications, and Performance Regulation of Single-Atom Catalysts. *Adv. Funct. Mater.* **2021**, *31* (12), 2008318.
- (12) Boukhvalov, D. W.; Katsnelson, M. I. Chemical Functionalization of Graphene with Defects. *Nano Lett.* **2008**, *8* (12), 4373–4379.
- (13) Liang, C.; Li, Z.; Dai, S. Mesoporous Carbon Materials: Synthesis and Modification. *Angew. Chemie Int. Ed.* **2008**, *47* (20), 3696–3717.
- (14) Lui, C. H.; Liu, L.; Mak, K. F.; Flynn, G. W.; Heinz, T. F. Ultraflat Graphene. *Nature* **2009**, *462* (7271), 339–341.
- (15) Chen, D.; Feng, H.; Li, J. Graphene Oxide: Preparation, Functionalization, and Electrochemical Applications. *Chem. Rev.* **2012**, *112* (11), 6027–6053.
- (16) Szabó, T.; Berkesi, O.; Forgó, P.; Josepovits, K.; Sanakis, Y.; Petridis, D.; Dékány, I. Evolution of Surface Functional Groups in a Series of Progressively Oxidized Graphite

- Oxides. *Chem. Mater.* **2006**, *18* (11), 2740–2749.
- (17) Compton, O. C.; Nguyen, S. T. Graphene Oxide, Highly Reduced Graphene Oxide, and Graphene: Versatile Building Blocks for Carbon-Based Materials. *Small* **2010**, *6* (6), 711–723.
- (18) Petek, U.; Ruiz-Zepeda, F.; Bele, M.; Gaberšček, M. Nanoparticles and Single Atoms in Commercial Carbon-Supported Platinum-Group Metal Catalysts. *Catalysts* **2019**, *9* (2), 134.
- (19) Serp, P. Cooperativity in Supported Metal Single Atom Catalysis. *Nanoscale* **2021**, *13* (12), 5985–6004.
- (20) Xi, J.; Sun, H.; Wang, D.; Zhang, Z.; Duan, X.; Xiao, J.; Xiao, F.; Liu, L.; Wang, S. Confined-Interface-Directed Synthesis of Palladium Single-Atom Catalysts on Graphene/Amorphous Carbon. *Appl. Catal. B Environ.* **2018**, *225*, 291–297.
- (21) Zhou, S.; Bongiorno, A. Density Functional Theory Modeling of Multilayer “Epitaxial” Graphene Oxide. *Acc. Chem. Res.* **2014**, *47* (11), 3331–3339.
- (22) Guilhon, I.; Bechstedt, F.; Botti, S.; Marques, M.; Teles, L. K. Chemically Tunable Properties of Graphene Covered Simultaneously with Hydroxyl and Epoxy Groups. *J. Phys. Chem. C* **2017**, *121* (49), 27603–27611.
- (23) Kresse, G.; Furthmüller, J. Efficiency of Ab-Initio Total Energy Calculations for Metals and Semiconductors Using a Plane-Wave Basis Set. *Comput. Mater. Sci.* **1996**, *6* (1), 15–50.

- (24) Kresse, G.; Furthmüller, J. Efficient Iterative Schemes for Ab Initio Total-Energy Calculations Using a Plane-Wave Basis Set. *Phys. Rev. B* **1996**, *54* (16), 11169–11186.
- (25) Perdew, J. P.; Burke, K.; Ernzerhof, M. Generalized Gradient Approximation Made Simple. *Phys. Rev. Lett.* **1996**, *77* (18), 3865–3868.
- (26) Grimme, S.; Antony, J.; Ehrlich, S.; Krieg, H. A Consistent and Accurate Ab Initio Parametrization of Density Functional Dispersion Correction (DFT-D) for the 94 Elements H-Pu. *J. Chem. Phys.* **2010**, *132* (15), 154104.
- (27) Blöchl, P. E. Projector Augmented-Wave Method. *Phys. Rev. B* **1994**, *50* (24), 17953–17979.
- (28) Kresse, G.; Joubert, D. From Ultrasoft Pseudopotentials to the Projector Augmented-Wave Method. *Phys. Rev. B* **1999**, *59* (3), 1758–1775.
- (29) Monkhorst, H. J.; Pack, J. D. Special Points for Brillouin-Zone Integrations. *Phys. Rev. B* **1976**, *13* (12), 5188–5192.
- (30) Nosé, S. A Molecular Dynamics Method for Simulations in the Canonical Ensemble. *Mol. Phys.* **1984**, *52* (2), 255–268.
- (31) Deringer, V. L.; Tchougréeff, A. L.; Dronskowski, R. Crystal Orbital Hamilton Population (COHP) Analysis as Projected from Plane-Wave Basis Sets. *J. Phys. Chem. A* **2011**, *115* (21), 5461–5466.
- (32) Maintz, S.; Deringer, V. L.; Tchougréeff, A. L.; Dronskowski, R. Analytic Projection from Plane-Wave and PAW Wavefunctions and Application to Chemical-Bonding Analysis in

- Solids. *J. Comput. Chem.* **2013**, *34* (29), 2557–2567.
- (33) Dronskowski, R.; Blöchl, P. E. Crystal Orbital Hamilton Populations (COHP): Energy-Resolved Visualization of Chemical Bonding in Solids Based on Density-Functional Calculations. *J. Phys. Chem.* **1993**, *97* (33), 8617–8624.
- (34) Giannozzi, P.; Baroni, S. Vibrational and Dielectric Properties of C60 from Density-Functional Perturbation Theory. *J. Chem. Phys.* **1994**, *100* (11), 8537–8539.
- (35) Porezag, D.; Pederson, M. R. Infrared Intensities and Raman-Scattering Activities within Density-Functional Theory. *Phys. Rev. B* **1996**, *54* (11), 7830–7836.
- (36) Stone, A. J.; Wales, D. J. Theoretical Studies of Icosahedral C60 and Some Related Species. *Chem. Phys. Lett.* **1986**, *128* (5), 501–503.
- (37) Krasheninnikov, A. V.; Lehtinen, P. O.; Foster, A. S.; Nieminen, R. M. Bending the Rules: Contrasting Vacancy Energetics and Migration in Graphite and Carbon Nanotubes. *Chem. Phys. Lett.* **2006**, *418* (1), 132–136.
- (38) Lehtinen, P. O.; Foster, A. S.; Ayuela, A.; Krasheninnikov, A. V.; Nordlund, K.; Nieminen, R. M. Magnetic Properties and Diffusion of Adatoms on a Graphene Sheet. *Phys. Rev. Lett.* **2003**, *91* (1), 17202.
- (39) Krasheninnikov, A. V.; Lehtinen, P. O.; Foster, A. S.; Pyykkö, P.; Nieminen, R. M. Embedding Transition-Metal Atoms in Graphene: Structure, Bonding, and Magnetism. *Phys. Rev. Lett.* **2009**, *102* (12), 126807.
- (40) Lee, G.-D.; Wang, C. Z.; Yoon, E.; Hwang, N.-M.; Kim, D.-Y.; Ho, K. M. Diffusion,

- Coalescence, and Reconstruction of Vacancy Defects in Graphene Layers. *Phys. Rev. Lett.* **2005**, *95* (20), 205501.
- (41) Kotakoski, J.; Meyer, J. C.; Kurasch, S.; Santos-Cottin, D.; Kaiser, U.; Krasheninnikov, A. V. Stone-Wales-Type Transformations in Carbon Nanostructures Driven by Electron Irradiation. *Phys. Rev. B* **2011**, *83* (24), 245420.
- (42) Figueiredo, J. L. Functionalization of Porous Carbons for Catalytic Applications. *J. Mater. Chem. A* **2013**, *1* (33), 9351–9364.
- (43) Romanos, G. E.; Likodimos, V.; Marques, R. R. N.; Steriotis, T. A.; Papageorgiou, S. K.; Faria, J. L.; Figueiredo, J. L.; Silva, A. M. T.; Falaras, P. Controlling and Quantifying Oxygen Functionalities on Hydrothermally and Thermally Treated Single-Wall Carbon Nanotubes. *J. Phys. Chem. C* **2011**, *115* (17), 8534–8546.
- (44) Gerber, I. C.; Oubenali, M.; Bacsa, R.; Durand, J.; Gonçalves, A.; Pereira, M. F. R.; Jolibois, F.; Perrin, L.; Poteau, R.; Serp, P. Theoretical and Experimental Studies on the Carbon-Nanotube Surface Oxidation by Nitric Acid: Interplay between Functionalization and Vacancy Enlargement. *Chem. – A Eur. J.* **2011**, *17* (41), 11467–11477.
- (45) Mkhoyan, K. A.; Contryman, A. W.; Silcox, J.; Stewart, D. A.; Eda, G.; Mattevi, C.; Miller, S.; Chhowalla, M. Atomic and Electronic Structure of Graphene-Oxide. *Nano Lett.* **2009**, *9* (3), 1058–1063.
- (46) Luo, Z.; Vora, P. M.; Mele, E. J.; Johnson, A. T. C.; Kikkawa, J. M. Photoluminescence and Band Gap Modulation in Graphene Oxide. *Appl. Phys. Lett.* **2009**, *94* (11), 111909.

- (47) Si, Y.; Samulski, E. T. Synthesis of Water Soluble Graphene. *Nano Lett.* **2008**, *8* (6), 1679–1682.
- (48) Bagri, A.; Mattevi, C.; Acik, M.; Chabal, Y. J.; Chhowalla, M.; Shenoy, V. B. Structural Evolution During the Reduction of Chemically Derived Graphene Oxide. *Nat. Chem.* **2010**, *2* (7), 581–587.
- (49) Graf, D.; Molitor, F.; Ensslin, K.; Stampfer, C.; Jungen, A.; Hierold, C.; Wirtz, L. Spatially Resolved Raman Spectroscopy of Single- and Few-Layer Graphene. *Nano Lett.* **2007**, *7* (2), 238–242.
- (50) Kudin, K. N.; Ozbas, B.; Schniepp, H. C.; Prud'homme, R. K.; Aksay, I. A.; Car, R. Raman Spectra of Graphite Oxide and Functionalized Graphene Sheets. *Nano Lett.* **2008**, *8* (1), 36–41.
- (51) Rivera-Cárcamo, C.; Gerber, I. C.; del Rosal, I.; Guicheret, B.; Castro Contreras, R.; Vanoye, L.; Favre-Réguillon, A.; Machado, B. F.; Audevard, J.; de Bellefon, C.; Philippe, R.; Serp, P. Control of the Single Atom/Nanoparticle Ratio in Pd/C Catalysts to Optimize the Cooperative Hydrogenation of Alkenes. *Catal. Sci. Technol.* **2021**, *11* (3), 984–999.
- (52) Contreras, R. C.; Guicheret, B.; Machado, B. F.; Rivera-Cárcamo, C.; Curiel Alvarez, M. A.; Valdez Salas, B.; Rutttert, M.; Placke, T.; Favre Réguillon, A.; Vanoye, L.; de Bellefon, C.; Philippe, R.; Serp, P. Effect of Mesoporous Carbon Support Nature and Pretreatments on Palladium Loading, Dispersion and Apparent Catalytic Activity in Hydrogenation of Myrcene. *J. Catal.* **2019**, *372*, 226–244.
- (53) Rivera-Cárcamo, C.; Serp, P. Single Atom Catalysts on Carbon-Based Materials.

*ChemCatChem* **2018**, *10* (22), 5058–5091.

- (54) Skowron, S. T.; Lebedeva, I. V.; Popov, A. M.; Bichoutskaia, E. Energetics of Atomic Scale Structure Changes in Graphene. *Chem. Soc. Rev.* **2015**, *44* (10), 3143–3176.
- (55) Huang, X.; Yan, H.; Huang, L.; Zhang, X.; Lin, Y.; Li, J.; Xia, Y.; Ma, Y.; Sun, Z.; Wei, S.; Lu, J. Toward Understanding of the Support Effect on Pd1 Single-Atom-Catalyzed Hydrogenation Reactions. *J. Phys. Chem. C* **2019**, *123* (13), 7922–7930.
- (56) Yang, Y.; Castano, C. E.; Gupton, B. F.; Reber, A. C.; Khanna, S. N. A Fundamental Analysis of Enhanced Cross-Coupling Catalytic Activity for Palladium Clusters on Graphene Supports. *Nanoscale* **2016**, *8* (47), 19564–19572.
- (57) Zlotea, C.; Cuevas, F.; Paul-Boncour, V.; Leroy, E.; Dibandjo, P.; Gadiou, R.; Vix-Guterl, C.; Latroche, M. Size-Dependent Hydrogen Sorption in Ultrasmall Pd Clusters Embedded in a Mesoporous Carbon Template. *J. Am. Chem. Soc.* **2010**, *132* (22), 7720–7729.
- (58) Bugaev, A. L.; Guda, A. A.; Lomachenko, K. A.; Lazzarini, A.; Srabionyan, V. V.; Vitillo, J. G.; Piovano, A.; Groppo, E.; Bugaev, L. A.; Soldatov, A. V.; Dmitriev, V. P.; Pellegrini, R.; van Bokhoven, J. A.; Lamberti, C. Hydride Phase Formation in Carbon Supported Palladium Hydride Nanoparticles by in Situ EXAFS and XRD. *J. Phys. Conf. Ser.* **2016**, *712*, 12032.
- (59) Wang, L.-L.; Johnson, D. D. Shear Instabilities in Metallic Nanoparticles: Hydrogen-Stabilized Structure of Pt<sub>37</sub> on Carbon. *J. Am. Chem. Soc.* **2007**, *129* (12), 3658–3664.
- (60) Wang, L.-L.; Johnson, D. D. Density Functional Study of Structural Trends for Late-

- Transition-Metal 13-Atom Clusters. *Phys. Rev. B* **2007**, 75 (23), 235405.
- (61) del Rosal, I.; Jolibois, F.; Maron, L.; Philippot, K.; Chaudret, B.; Poteau, R. Ligand Effect on the NMR, Vibrational and Structural Properties of Tetra- and Hexanuclear Ruthenium Hydrido Clusters: A Theoretical Investigation. *Dalt. Trans.* **2009**, No. 12, 2142–2156.
- (62) Zhou, C.; Szpunar, J. A. Hydrogen Storage Performance in Pd/Graphene Nanocomposites. *ACS Appl. Mater. Interfaces* **2016**, 8 (39), 25933–25940.
- (63) Berthoud, R.; Délichère, P.; Gajan, D.; Lukens, W.; Pelzer, K.; Basset, J.-M.; Candy, J.-P.; Copéret, C. Hydrogen and Oxygen Adsorption Stoichiometries on Silica Supported Ruthenium Nanoparticles. *J. Catal.* **2008**, 260 (2), 387–391.
- (64) García-Antón, J.; Axet, M. R.; Jansat, S.; Philippot, K.; Chaudret, B.; Pery, T.; Buntkowsky, G.; Limbach, H.-H. Reactions of Olefins with Ruthenium Hydride Nanoparticles: NMR Characterization, Hydride Titration, and Room-Temperature C-C Bond Activation. *Angew. Chemie Int. Ed.* **2008**, 47 (11), 2074–2078.
- (65) Mager-Maury, C.; Bonnard, G.; Chizallet, C.; Sautet, P.; Raybaud, P. H<sub>2</sub>-Induced Reconstruction of Supported Pt Clusters: Metal–Support Interaction versus Surface Hydride. *ChemCatChem* **2011**, 3 (1), 200–207.
- (66) Jen, P.-H.; Hsu, Y.-H.; Lin, S. D. The Activity and Stability of Pd/C Catalysts in Benzene Hydrogenation. *Catal. Today* **2007**, 123 (1), 133–141.
- (67) Dong, W.; Ledentu, V.; Sautet, P.; Eichler, A.; Hafner, J. Hydrogen Adsorption on Palladium: A Comparative Theoretical Study of Different Surfaces. *Surf. Sci.* **1998**, 411 (1),

123–136.

- (68) Cusinato, L.; Martínez-Prieto, L. M.; Chaudret, B.; del Rosal, I.; Poteau, R. Theoretical Characterization of the Surface Composition of Ruthenium Nanoparticles in Equilibrium with Syngas. *Nanoscale* **2016**, *8* (21), 10974–10992.
- (69) Andrews, L. Matrix Infrared Spectra and Density Functional Calculations of Transition Metal Hydrides and Dihydrogen Complexes. *Chem. Soc. Rev.* **2004**, *33* (2), 123–132.
- (70) Andrews, L.; Wang, X.; Alikhani, M. E.; Manceron, L. Observed and Calculated Infrared Spectra of Pd(H<sub>2</sub>)<sub>1,2,3</sub> Complexes and Palladium Hydrides in Solid Argon and Neon. *J. Phys. Chem. A* **2001**, *105* (13), 3052–3063.